CPP

Contributions to Plasma Physics

www.cpp-journal.org

WILEY-VCH

REPRINT

Contrib. Plasma Phys. **52**, No. 10, 827 – 835 (2012) / **DOI** 10.1002/ctpp.201200039

Plasma Sheath Structures in Complex Electrode Geometries

G. Schubert[1]*, **M. Haass**[2]**, **T. Trottenberg**[2], **H. Fehske**[1], and **H. Kersten**[2]***

[1] Institut für Physik, Ernst-Moritz-Arndt-Universität Greifswald, 17487 Greifswald, Germany
[2] Institut für Experimentelle und Angewandte Physik, Christian-Albrechts-Universität zu Kiel, 24098 Kiel, Germany

Received 10 May 2012, revised 12 July 2012, accepted 12 July 2012
Published online 08 November 2012

Key words Plasma sheath, particle trapping, vertical wall, particle diagnostics.

The behavior of microparticles trapped in the curved plasma sheath in the corner of a horizontal rf electrode and a vertical wall is investigated by experiments and simulation. Three types of walls are studied, namely a dielectric wall, a floating conductive wall, and a conductive wall at the same potential as the rf electrode. The particle's equilibrium position provides insight in the acting forces, associated potentials and field structures. Complementary particle-in-cell simulations elucidate the structure of the charged-species densities and electric potential profile throughout the sheath. Thereby special emphasis is placed on how the sheath structure in the corner depends on the wall material.

1 Introduction

Interfaces between plasmas and electrodes, floating and biased (or grounded) surfaces are common in laboratory plasmas. Where the plasma meets such solid surfaces, a sheath forms and separates the quasi-neutral plasma from the wall. The typically only a few millimeters wide sheaths are characterized by a positive space charge, large potential drops and corresponding strong electric fields, which keep the electrons inside the plasma. Powered electrodes (PE) in radio-frequency (rf) discharges give rise to significantly higher voltage drops than floating or grounded walls. In case of a plane surface, the sheath is a one-dimensional phenomenon, and all quantities depend only on the distance to the surface. However, when a plasma is not bounded by simple geometries, e.g. by planes, cylinders or spheres, but limited by arbitrarily shaped three-dimensional surfaces of dielectrics and conductive walls at different potentials, the situation becomes much more involved.

Complex electrode geometries are often used in industrial applications, for example in plasma-immersion ion implantation, which allows for a treatment of irregularly shaped substrates [1]. In the experimental study of complex (dusty) plasma phenomena [2], complex electrode geometries are used as particle traps [3–5]. So far, the geometries themselves were rarely subject to research.

Diagnostics of plasma sheaths and their dependence on three-dimensional electrode geometry can hardly be done with Langmuir probes because of their disturbance. Recently, microparticles have been used as minimally invasive probes [6]. For example, the local electric field could be determined by particles trapped above an "adaptive electrode" and the result was successfully compared with simulations [7]. Energy fluxes to microparticles trapped in the same experimental setup have been studied using fluorescent particles, too [8].

Three years ago, Basner et al. [6] reported an interesting observation in a setup with a horizontal plane rf electrode and a vertical glass plate placed on the electrode: A cloud of microparticles trapped in the sheath in the corner of electrode and glass plate showed a behavior which reminds of the wetting of surfaces immersed into liquids. The authors presented a simple model for this behavior which takes into account electrostatic forces between surface charges on the wall and the charged microparticles.

* The author is now with Philips Healthcare, Äyritie 4, 01510 Vantaa, Finland
** The author is now with LTM (CNRS/UJF-Grenoble1/CEA), 17 avenue des Martyrs, 38054 Grenoble cedex 9, France
*** Corresponding author. E-mail: kersten@physik.uni-kiel.de, Phone: +49 431 880 3872, Fax: +49 431 880 3809

In this contribution, we extend the investigation of this phenomenon by systematic experiments and particle-in-cell (PIC) simulations [9]. Besides a dielectric glass wall, metal walls at rf or floating potential are used. Instead of a particle cloud, we observe single particles in order to exclude particle-particle interactions, which would make the physics even more intricate. By these investigations the concept of "particles as probes" combines typical phenomena of dusty plasmas [2, 10–12] with rf plasma diagnostics [13].

2 Experimental Setup

The experimental setup is a typical capacitively coupled rf discharge configuration used in many dusty plasma experiments where particles are trapped in the sheath above a powered horizontal electrode [14]. The rf electrode is a stainless steel disk of 140 mm diameter surrounded by a grounded guard ring [see Fig. 1a)]. The cylindrical vacuum vessel has a diameter of 400 mm and approximately the same height. The discharge is operated with argon at pressures in the range of $p = (10 - 30)$ Pa and rf powers in the range of $P = (10 - 70)$ W at a frequency of 13.56 MHz.

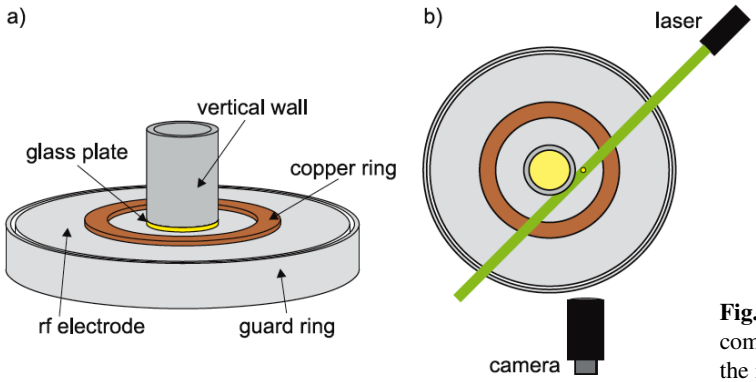

Fig. 1 Experimental setup. a) Schematic of the complex electrode geometry. b) Top view onto the rf electrode, the particles are illuminated by a slightly expanded laser beam.

The three-dimensional electrode geometry is realized by either conductive (metal) or dielectric (glass) cylinders which are placed at the center of the rf electrode (Fig. 1). The metal cylinder can be separated from the electrode by a 2 mm thick glass disk of the same diameter, or put directly on the electrode. In this way, the conductive wall is floating or connected to the rf voltage. The (hollow) cylinders have a diameter of $2r_c = 30$ mm and a height of $h = 40$ mm.

Three types of spherical particles were used: melamine formaldehyde (MF) spheres of diameter $d_1 = (5.26 \pm 0.08)\,\mu$m and $d_2 = (10.20 \pm 0.10)\,\mu$m, and hollow glass spheres with diameters of $d_3 = (99.4 \pm 13.4)\,\mu$m. In case of the MF particles with very narrow size distribution, the mass can be calculated with a small error, yielding masses of $m_1 = 1.15 \times 10^{-13}$ kg for the smaller and $m_2 = 8.39 \times 10^{-13}$ kg for the larger ones, respectively. The hollow glass spheres are a sample of the same particles analyzed earlier by Schneider et al. [15] and have a mass of $m_3 = (5 \pm 2.3) \times 10^{-11}$ kg.

The particles are injected into the plasma by a dust dropper, a small container with 300 μm opening that is vertically shaken. The released particles, which become negatively charged in the plasma, are stopped and suspended in the sheath above the electrode. In order to avoid that the particles escape laterally over the border of the electrode, a 2 mm flat ring of copper with inner diameter of 63 mm is put on the electrode and deforms the sheath to a radially confining low bank. The ring affects the sheath only in the vicinity of a few millimeters. Even though the azimuthal position is not constricted in our axisymmetric setup, the particles always move after their injection slowly to the same azimuthal position. This for the observation advantageous behavior can be attributed to a weak neutral gas flow, which is negligible for the equilibrium position in the observation plane.

The trapped particles are illuminated with the radially slightly expanded beam generated by a frequency doubled laser diode with a wavelength of 532 nm and a power of 10 mW [see Fig. 1b)]. The scattered light is observed under an angle of 135 degrees by a charged-coupled device (ccd) camera with a resolution of 1600×1200 pixels equipped with a $f = (13 - 130)$ mm zoom lens. Figure 2 shows typical camera images.

The discharge was characterized by Langmuir probe measurements and monitoring of the global quantities of the electric circuit, in order to obtain reliable input parameters for the model. For increasing rf powers in the range $P = (10 - 70)$ W, the rf voltage amplitude increases in the range $\Phi \approx (125 - 700)$ V (peak-to-peak), with some variations for the different cylinders and pressures. The self-bias of the rf electrode is in the range $\Phi_{\rm bias} = -(30 - 280)$ V. The cylindrical Langmuir probe, with a tungsten wire of 1.5 mm length as active probe tip, is passively filtered at the rf frequency and its first harmonic, and is biased via a capacitor by a reference electrode that picks up the rf plasma potential variations [16–18]. In our design, the reference electrode is a steel tube with an active length of 7 mm which shortly behind the probe tip encloses the ceramic tube that covers the probe lead. It was ensured that the few injected microparticles did not fall onto the probe tip in order to avoid systematic errors due to deposition of dust grains. It is well known that such contaminations in complex plasmas reduce significantly the active area of the probe surface [19]. The measured plasma potential depends only slightly on gas pressure and rf power in the considered parameter ranges and remains always between $\Phi_{\rm pl} = (28 - 34)$ V. The electron density increases from $n_{\rm e} = 0.5 \times 10^{15}\,{\rm m}^{-3}$ for $P = 10$ W to $n_{\rm e} = 12 \times 10^{15}\,{\rm m}^{-3}$ for $P = 70$ W, while the pressure dependence is insignificant. The electron temperature is in the range of $T_{\rm e} = (2.5 - 5)$ eV. It decreases with increasing rf voltage and is generally higher for higher pressures.

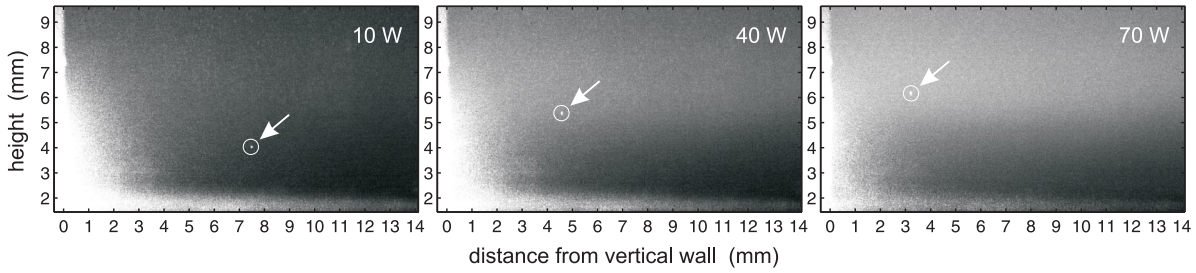

Fig. 2 Camera images of a single 10-μm melamine formaldehyde particle trapped beside a glass cylinder at a gas pressure of $p = 21.1$ Pa. Each image corresponds to one of the rf powers $P = 10$ W, 40 W, and 70 W as indicated by the labels.

3 Experimental Observations

In this section, the particle's equilibrium positions are determined experimentally for a) the glass cylinder, b) the floating steel cylinder and c) the steel cylinder in electrical contact with the rf electrode. The measurements are summarized in the three corresponding Figs. 3a) to 3c). For each wall-particle combination, a gas pressure is chosen and the rf power is varied, resulting in the displayed sets of isobaric curves. The curves are traversed four times during several minutes in order to obtain the statistical errors for reproducibility shown in the figure.

Glass cylinder. In case of the glass cylinder as vertical wall, all the graphs show an identical feature: with increasing rf power, the equilibrium positions shift toward the glass wall and to increased heights above the rf electrode [Fig. 3a)]. The isobaric curves do not intersect and are closer to the corner, i.e. less distant to both walls, for higher pressures.

There is a slightly different behavior for the three particle types. Compared to the 10 μm particles, the smaller MF particles find equilibrium positions a little higher. The closer the particles come to the wall, the more they move vertically, i.e. parallel to the dielectric wall, when the rf power changes. The hollow glass spheres get even closer to the glass wall. In contrast to the 5 μm MF particles, the curves remain straight, regardless of the proximity to the wall. In the case of the two higher pressures, $p = 21.1$ Pa and $p = 25.4$ Pa, the spheres even reach the glass cylinder at lower rf powers ($P < 70$ W) and get lost. For this reason, only two curves are plotted for the hollow glass spheres.

Floating steel cylinder. In case of the floating steel cylinder as vertical wall, the particles maintain generally a larger distance to the wall than in case of the glass wall [Fig. 3b)]. This enables an observation of the hollow glass spheres at higher rf powers and higher pressures.

The 5 μm MF particles move at larger distances from the wall almost horizontally, but the closer the particles come to the wall for increasing powers, the stronger becomes the component parallel to the vertical wall. Surprisingly, the isobaric lines for the 10 μm MF particles are opposedly curved. The curves for the hollow spheres seem to combine both features and are slightly s-shaped.

Steel cylinder at rf potential. Finally, the steel cylinder at the same potential as the horizontal rf electrode produces isobaric lines which are predominantly vertical [Fig. 3c)]. The particle distances to the vertical wall are now significantly larger than the heights above the horizontal electrode. Since in this case the particles are only about 2 mm away from the copper ring that provides the outer confinement, one can conjecture that there is a strong repelling force away from the vertical rf wall.

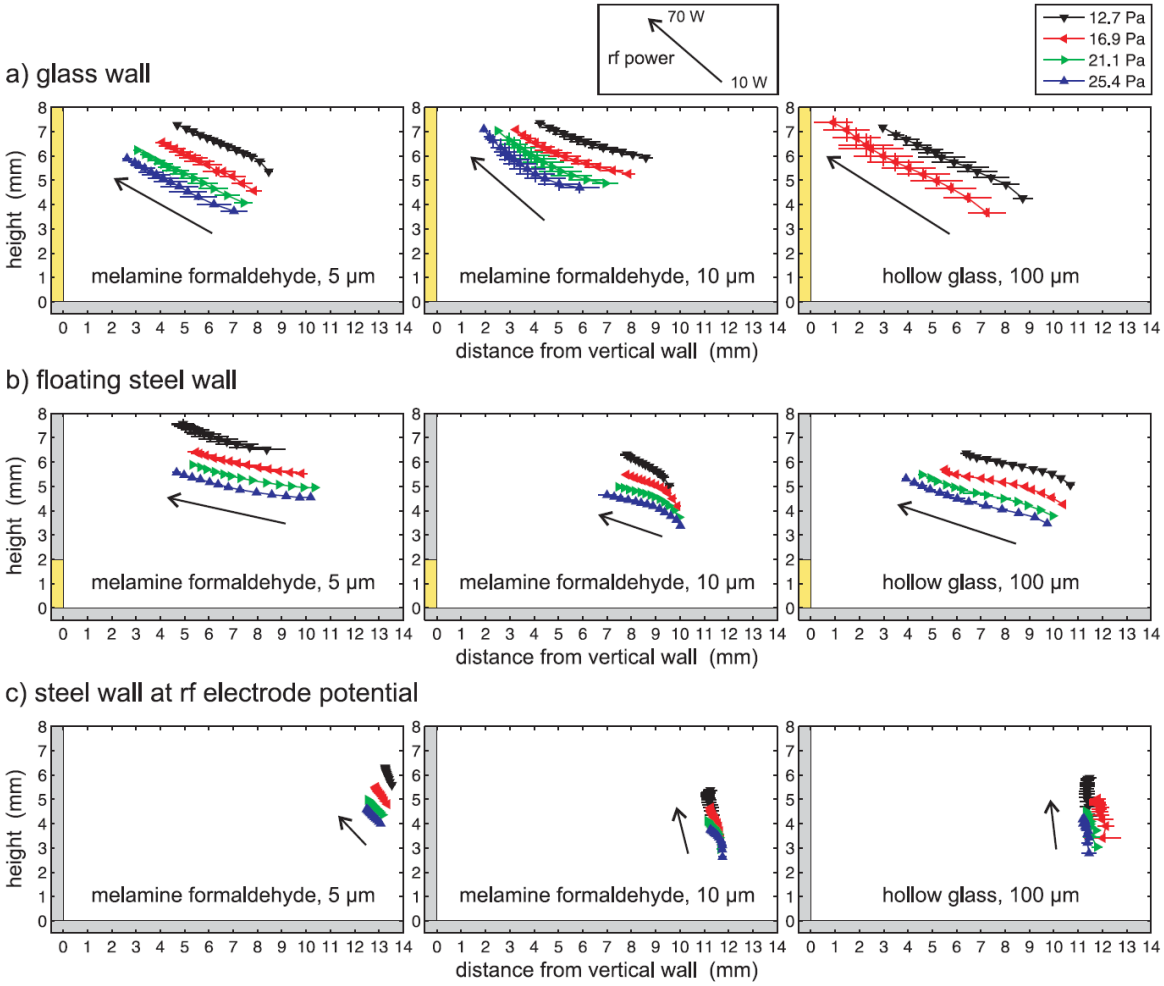

Fig. 3 Measured equilibrium positions of spherical particles of three different types. The vertical wall is a) a dielectric, b) a floating conductor, and c) a conductor connected to the rf electrode. The discharge power was increased from 10 W to 70 W as indicated by the arrows. The data points connected by lines correspond to different rf powers at the same pressure.

4 Simulations

Concomitantly and complementary to the experiment we simulate the sheath structure in the vicinity of the cylinder numerically. Thereby, we restrict ourselves to the glass cylinder and the metal cylinder in contact with the

electrode. Quantities of interest are the local electron and ion densities, the electrostatic potential and the accumulated net charge on the glass cylinder. In order to access the full kinetic information we model the discharge using a PIC technique. In doing so, we fully account for non-equilibrium effects by calculating the phase-space distributions of both charged species self-consistently [6]. Based on the sheath profile and the spatially resolved ion velocity, we may also estimate the particle charge, e.g., within the orbital motion limit theory. In total, this allows for determining the electric field force and ion drag force throughout the sheath region and consequently the particle equilibrium position.

All presented simulation results have been calculated using an electrostatic $2d(r,z)3v$ PIC code, that is based on the one used in [7], where also a more detailed description can be found. The relevant modifications in order to adapt the code to this experimental setup are summarized in the following.

We restrict the simulation volume to a $40\,\mathrm{mm} \times 40\,\mathrm{mm}$ rectangle aligned with the powered electrode and the cylinder wall. Using 800×800 grid points we ensure that the grid spacing resolves scales of half of the Debye length. The time step is adapted according to the plasma parameters in order to resolve $1/5$ of the inverse plasma frequency. Respecting these constraints is mandatory for the PIC method to provide reliable results [20].

The simulation volume is bounded by an absorbing wall at the top boundary and reflecting boundary conditions with vanishing electric field at the outer boundary in radial direction. Our exclusive interest in the sheath in the PE / cylinder corner justifies the use of such a substitute setup as long as the bulk plasma properties match the experimental ones. We ensure this agreement by tuning the substitute control parameters and confirm independence between corner sheath properties and used outer boundary conditions. It is evident, that the larger the substitute volume is chosen, the better the bulk parameters can be matched. For the used substitute volume we achieve an agreement with the experimental values better than 5% for densities and plasma potential. Calculated electron temperatures underestimate the experimental values by up to 10%.

Depending on the cylinder material we choose the solution method for Poisson's equation. For the metal cylinder, cyclic reduction is directly applicable. The dielectric cylinder case requires a combination of cyclic reduction with a relaxation method. Starting out from the cyclic reduction solution as initial guess, the latter is used to incorporate the effect of a finite charge density at the cylinder surface and its different dielectric constant.

As before [6,7], we adopt a point of view in which the disturbance of the plasma parameters by the test particle is neglected. This approach is consistent with the notion of using 'particles as probes'. Instead of explicitly resolving the particle charging, we exploit the faster dynamics of the sheath formation and estimate the particle's acquired charge from the local conditions in its surrounding.

5 Simulation results

Other than the experimental particle positions, the PIC simulation provides high-resolution data on the plasma parameters throughout the sheath. This is of particular interest with respect to the different spatial sheath structures in the corner for both the metal and glass cylinder as shown in Fig. 4. Since the connected metal cylinder is on the same potential as the PE, the horizontal and vertical sheath structures correspond. The symmetry of the depicted ion velocities underlines that the metal cylinder acts just like a prolongation of the PE. This is in contrast to the case of the glass cylinder. Here the sheaths in front of PE and cylinder differ markedly, mainly because of the discrepancy between arising self-bias and floating potential at the cylinder surface. The latter is slightly positive and position dependent, as will be discussed in more detail below. The strong electric fields generated by the potential differences in the vicinity of the corner locally sweep most electrons from that region. In this sense, the corner between PE and dielectric cylinder acts like an additionally negatively biased region. Away from the immediate corner, electron and ion density profiles are less steep toward the cylinder than toward the PE due to the reduced potential difference. Naturally, the same holds for the ion velocity.

In order to investigate these phenomena on a more quantitative level, Fig. 5 shows horizontal cuts through the data presented in Fig. 4 for different heights z above the PE. Thereby, we also address the question how the sheath profile changes as a function of plasma parameters. We elaborate these tendencies on the basis of selected results for representative parameters in the three columns of Fig. 5. For the metal cylinder, we do not observe any pronounced pressure dependence of the sheath parameters, which is consistent with the rather insensitive particle equilibrium positions in this case [Fig.3c)]. Increasing the rf power leads to a narrowing of the sheath in accordance with the shifting of the particle equilibrium positions towards the cylinder wall. In case of the

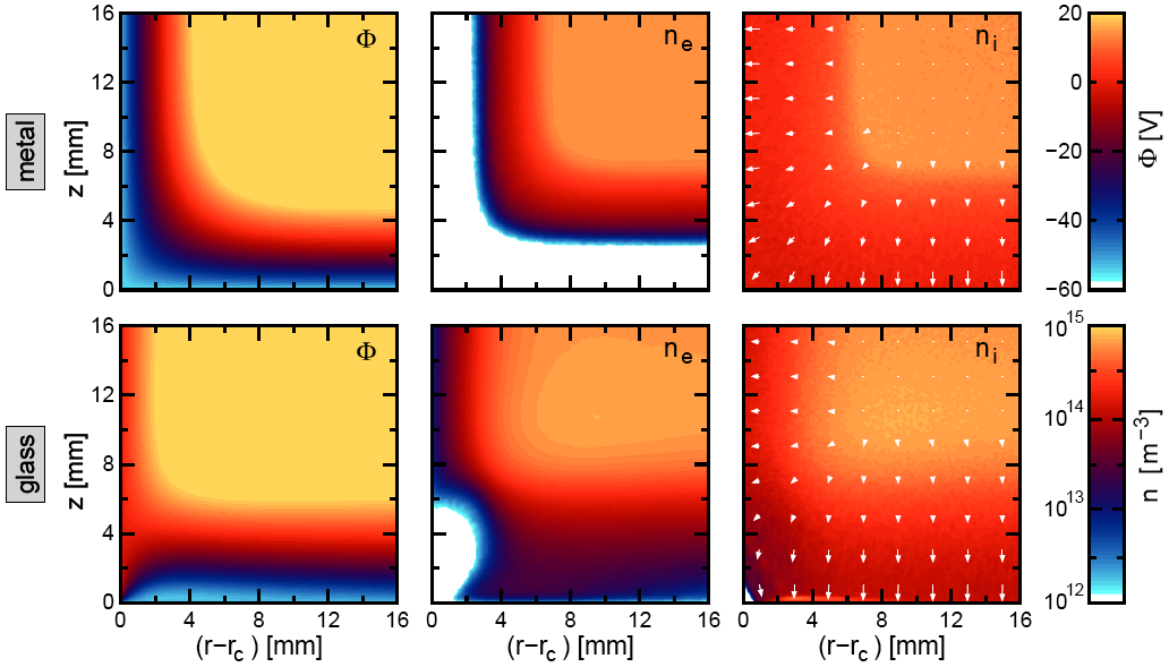

Fig. 4 Spatial profile of potential, electron and ion density in front of a metal (top row) and glass (bottom row) cylinder put on top of the powered rf electrode. In the ion density subpanels the arrows indicate direction and magnitude of the averaged ion velocity. Data obtained by PIC simulation; only part of the volume is shown: $p = 12.7\,\mathrm{Pa}$, $P = 10\,\mathrm{W}$.

glass cylinder, the selected heights for the cuts resolve both the electron deprived region near the corner and the plain cylinder above. As compared to the metal case, this explains the more pronounced height dependence of the density and potential profiles in the first column of Fig. 5. Enhancing the pressure results in a noticeable increase of the plasma potential and a reduction of the sheath width. Simultaneously, the electron deprivation is less pronounced because of the reduced sheath width. Also for the glass cylinder, increasing the rf power reduces the sheath width more drastically than any pressure changes which is again consistent with the results on the particle equilibrium positions in Fig.3a). Let us come back to the question how accumulated charges are distributed on the glass cylinder surface and what the resulting local floating potential is. The dielectric properties of glass efficiently hinder a charge equilibration on the cylinder surface and thus a spatially anisotropic charge profile and floating potential will arise. In Fig. 6 those quantities are given for the plasma parameters investigated in Fig. 5. Common to all cases is the maximum of accumulated negative charges around $z \approx 4\,\mathrm{mm}$. This height agrees roughly with the region where the electron density in the sheath is distinctly reduced due to the high field created by the PE. An attachment closer to the corner is impeded by the large vertical component of the electric field force. With increasing distance from the corner, the accumulated net charge decreases and approaches a constant value far from the PE. The markedly increased surface charge for $P = 70\,\mathrm{W}$ reflects the higher bulk density in this case. In addition to the influence of the surface charge, the local floating potential also reflects the electrostatic influence of the strongly self-biased PE, see right panel of Fig. 6. Near the corner the cylinder potential is markedly negative and attains positive values only for larger values of z. There it reflects the surface charge distribution and decays from its maximum value around $z \approx 4\,\mathrm{mm}$ to a stationary floating potential at large z.

Finally, we exploit the numerically obtained sheath structure to calculate the equilibrium positions of different test particles. Analogously to Ref. [7], we calculate the relevant contributions from gravity, electrostatic field force and ion drag force [10, 11]. The only free parameter entering the equilibrium position that is not captured directly in the PIC simulation is the particle charge. Taking the concept of 'particles as probes' seriously, we seek for the equilibrium positions of various particles with fixed charges. From these curves the relevant position can be extracted as soon as the actual particle charge is estimated by an applicable charging model (orbital motion limit theory, radial motion theory, etc.). For the metal cylinder setup we were not able to reliably determine a

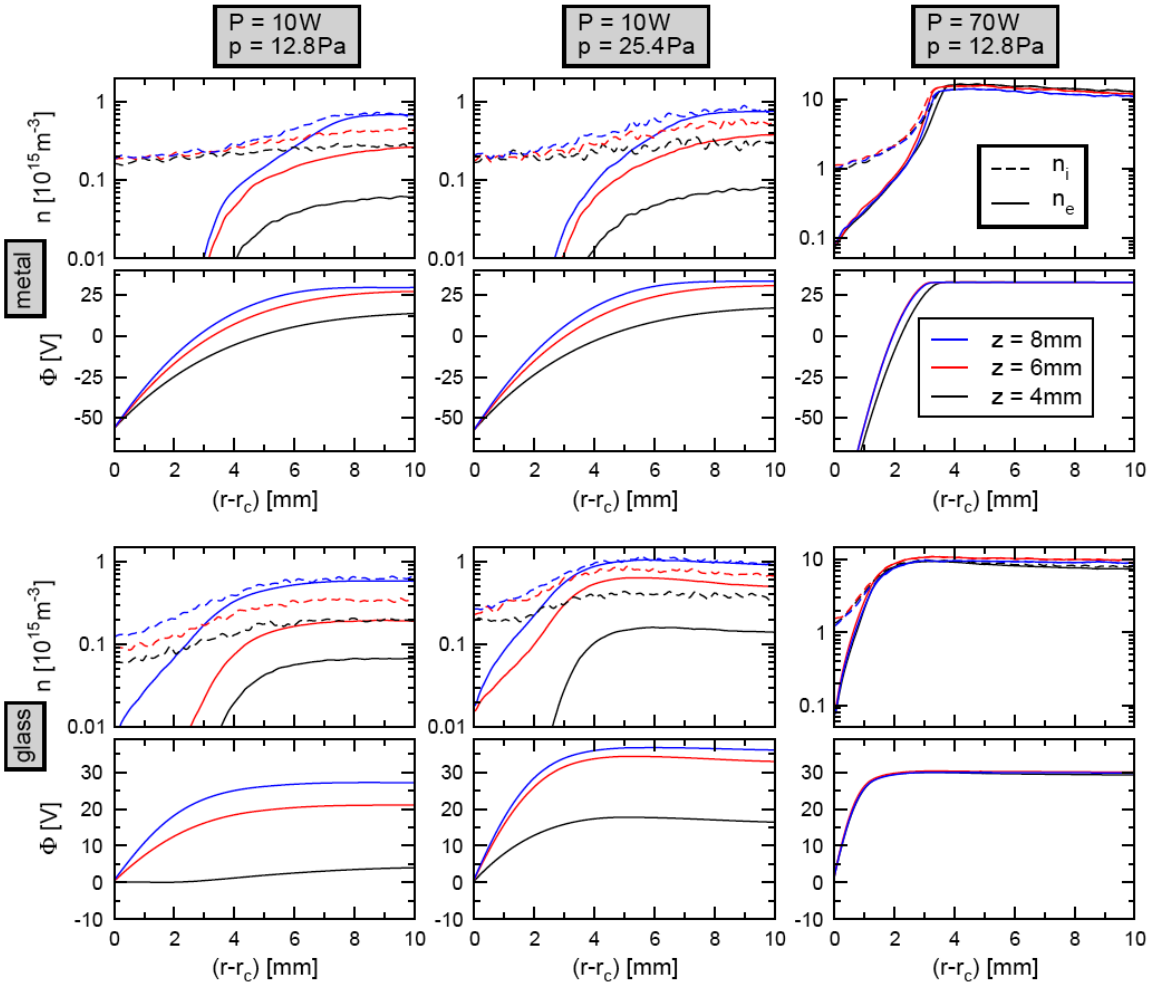

Fig. 5 Horizontal structure of the plasma sheath in dependence on pressure and supplied power. For the glass and the metal cylinder geometry and each set of control parameters the potential and charge carrier densities are given for different heights z above the rf electrode. Data obtained by PIC simulation.

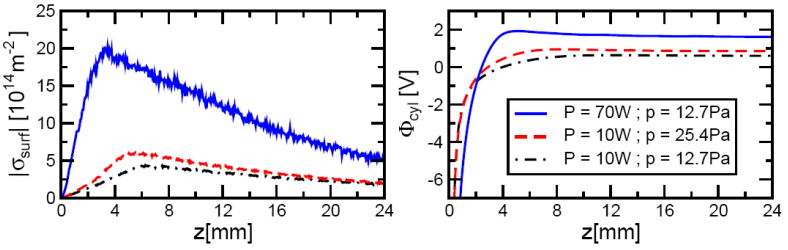

Fig. 6 Left panel: Net accumulated charge density on the glass cylinder as a function of vertical position. Right panel: Surface potential on the glass cylinder. Data obtained by PIC simulation.

distinct horizontal equilibrium position since the total force vanishes on a whole line (plane) parallel to the PE, see left panel of Fig. 7. Perpendicular to the PE we observe a pronounced minimum, but horizontally this trench is flat over several millimeters and local minima are only due to numerical fluctuations. This asymmetry is due to gravity counteracting the electric field force in vertical direction. Horizontally, the ion drag force is at no point strong enough to compete with the electric field force, and an equilibrium is only possible where the field of the cylinder is sufficiently shielded. Presumably, the well defined equilibrium positions found experimentally are imposed by the field of the copper ring, which is absent in our simulation. At a certain distance from the glass cylinder also a similar trench of vanishing force exists. In addition, near the cylinder wall a clearly separated local minimum

emerges for a certain range of particle charges, see right panel of Fig. 7. As a global trend we observe that the higher a particle is charged, the more its equilibrium plane shifts towards larger z. There, the weaker electric field compensates the effect of the increased charge. For the pressure dependence of the equilibrium positions, we achieve qualitative agreement with the tendencies observed in experiment. Quantitatively the distance from the cylinder wall is underestimated in the simulation results for the glass cylinder. A possible explanation might be the incomplete modeling of the cylinder wall charging. For increasing rf power the simulation reproduces the observed attraction towards the cylinder wall, but fails to capture the enhanced repelling of the PE. Apparently, this contradiction is due to the narrowing of the sheath in front of the PE as obtained by our simulation. At the highest simulated power levels the neglect of Coulomb collisions is seemingly no longer justified which offers a route of for improving the simulations.

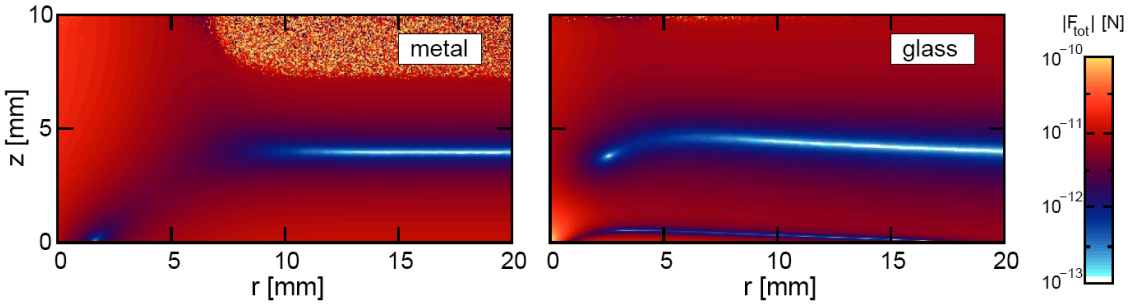

Fig. 7 Magnitude of total acting force on a $d = 10\,\mu$m particle with $Q = -5000e_0$ in front of a metal (left) and glass (right) cylinder. Data obtained by PIC simulation; $p = 12.7$ Pa, $P = 10$ W.

6 Outlook

We studied the behavior of microparticles trapped in the curved plasma sheath in the corner of a horizontal rf electrode and a vertical wall in dependence on the discharge conditions, e.g. gas pressure and discharge power. Three types of wall materials have been realized: floating (dielectric or metallic) cylinders and a conductive cylinder at the same potential as the flat metallic rf electrode. In order to obtain a better understanding of the phenomena, experiments are combined with theoretical modeling and numerical simulations of the geometric situation. Special attention is put on the particle positions related to the plasma sheath dynamics.

In case of the floating glass cylinder, the equilibrium positions of the particles shift for increasing power toward the glass wall and away from the rf electrode. If the floating metal cylinder is used, the particles remain farther away from the cylinder than in case of the dielectric. For the metal cylinder contacted to the rf electrode, the equilibrium positions are vertically aligned at a large distance from the wall.

The observed particles' equilibrium positions can be qualitatively explained by the superposed fields of the sheaths generated by the rf electrode and the wall, respectively, as well as by the drag due to the streaming ions through these sheaths. The simulations of the spatial potentials and charge carrier density profiles in front of the three-dimensional structures support the experimental observations and provide interesting information on the plasma parameter by comparison.

In case of the metal-cylinder setup we gained insight into the relative strength of the acting forces from the change of the equilibrium positions upon varying rf power. The key feature thereby is the breaking of the horizontally/vertically symmetric electric forces by gravity. The observed anisotropic charge distribution on the glass cylinder sheds a light on how sensibly charging depends on the local plasma conditions. As a consequence it should be carefully investigated up to which size the charge on microparticles may be treated as homogeneous.

The investigated effects are of high relevance for technological plasma processes, like physically enhanced chemical vapor deposition, magnetron sputtering [21,22] and plasma ion immersion implantation. Here, complex electrode geometries (holes, corners, edges) can be used to tailor the sheath properties and deposition patterns. Similar to our previous studies, the utilization of charged test particles in locally altered plasma sheath environments is a promising method for the characterization of electric field structures and plasma density profiles.

The results obtained in this work suggest further studies along two major directions:

(i) A more detailed investigation how sophisticated plasma sources affect the plasma properties would be of interest both in view of basic phenomena and technological applications. The implementation of a dual-frequency CCP discharge will allow for a separate control of ion flux and mean ion energy [23]. Combination of the rf plasma with a hollow cathode or magnetron discharge, which is common in deposition of nano-composite films [24] provides hints for the generation and transport of nanoparticles related to investigations by [21, 22].

(ii) Extending studies on particles in front of three-dimensional electrodes will improve the current understanding of particle charging processes. The wider range of available plasma parameters that can be realized in such geometries, e.g., by additional biasing or shape tuning, permits a detailed investigation of Coulombic interaction between plasma constituents and microparticles. By probing the sheath structure the charging mechanism can be studied precisely and compared to theoretical models [25] which are under investigation by [26].

As indicated above, in close collaboration with other projects in the framework of the Transregional Collaborative Research Center 24 called "Fundamentals of Complex Plasma" perfect conditions and possibilities exist to achieve the objectives.

Acknowledgements The technical assistance of Michael Poser and Volker Rohwer is gratefully acknowledged. This work was supported by DFG, SFB TR-24, projects A5 and B4.

References

[1] J. Conrad, J.L. Radtke, R.A. Dodd, F.J. Worzala, and N.C. Tran, J. Appl. Phys. **62**, 4591 (1987).
[2] J. Meichsner et al., Contrib. Plasma Phys. **52**, 789 (2012).
[3] B.M. Annaratone, M. Glier, T. Stuffler, M. Raif, H. M. Thomas, and G. E. Morfill, New J. Phys. **5**, 92 (2003).
[4] O. Arp, D. Block, and A. Piel, Phys. Rev. Lett. **93**, 165004 (2004).
[5] T. Trottenberg, D. Block, and A. Piel, Phys. Plasmas **13**, 042105 (2006).
[6] R. Basner, F. Sigeneger, D. Loffhagen, G. Schubert, H. Fehske, and H. Kersten, New J. Phys. **11**, 013041 (2009).
[7] G. Schubert, R. Basner, H. Kersten, and H. Fehske, Eur. Phys. J. D **63**, 431 (2011).
[8] H.R. Maurer, M. Hannemann, R. Basner, and H. Kersten, Phys. Plasmas **17**, 113707 (2010).
[9] T. Trottenberg, M. Haass, and H. Kersten, AIP Conf. Proc. **1397**, 333 (2011).
[10] D. Block, J. Cartensen, P. Ludwig, W.J. Miloch, F. Greiner, A. Piel, M. Bonitz, and A. Melzer, Contrib. Plasma Phys. **52**, 804 (2012).
[11] A. Melzer, A. Schella, T. Miksch, J. Schablinski,D. Block, A. Piel, H. Thomsen, H. Kählert, and M. Bonitz, Contrib. Plasma Phys. **52**, 795 (2012).
[12] T. Reichstein, J. Wilms, F. Greiner, A. Piel, and A. Melzer, Contrib. Plasma Phys. **52**, 813 (2012).
[13] C. Küllig, K. Dittmann, T. Wegner, I. Sheykin, K. Matyash, D. Loffhagen, R. Schneider, and J. Meichsner, Contrib. Plasma Phys. **52**, 836 (2012).
[14] T. Trottenberg, A. Melzer, and A. Piel, Plasma Sources Sci. Technol. **4**, 450 (1995).
[15] V. Schneider, T. Trottenberg, I. Teliban, and H. Kersten, Rev. Sci. Instrum. **81**, 013503 (2010).
[16] R.R.J. Gagné and A. Cantin, J. Appl. Phys. **43**, 2639 (1972).
[17] V.A. Godyak, R.B. Piejak, and B.M. Alexandrovich, J. Appl. Phys. **73**, 3657 (1993).
[18] V.A. Godyak and V.I. Demidov, J. Phys. D: Appl. Phys. **44**, 233001 (2011).
[19] T. Trottenberg, B. Brede, D. Block, and A. Piel, Phys. Plasmas **10**, 4627 (2003).
[20] D. Tskhakaya, K. Matyash, R. Schneider, and F. Taccogna, Contrib. Plasma Phys. **47**, 563 (2007).
[21] M. Bonitz, L. Rosenthal, K. Fujioka, V. Zaporojtchenko, F. Faupel, and H. Kersten, Contrib. Plasma Phys. **52**, 890 (2012).
[22] M. Ganeva, T. Peter, S. Bornholdt, H. Kersten, T. Strunskus, V. Zaporojtchenko, F. Faupel, and R. Hippler, Contrib. Plasma Phys. **52**, 881 (2012).
[23] J. Schulze, E. Schüngel, and U. Czarnetzki, Appl. Phys. Lett. **100**, 024102 (2012).
[24] T. Peter, M. Wegner, V. Zaporojtchenko, T. Strunskus, S. Bornholdt, H. Kersten, and F. Faupel, Surf. Coat. Technol. **205**, S38 (2011).
[25] R.L. Heinisch, F.X. Bronold, and H. Fehske, Phys. Rev. B **85**, 075323 (2012).
[26] F.X. Bronold, H. Fehske, R. Heinisch, and J. Marbach, Contrib. Plasma Phys. **52**, 856 (2012).

